First result from the Alpha Magnetic Spectrometer on the International Space Station: Precision measurement of the positron fraction in primary cosmic rays of 0.5−350 GeV

M. Aguilar,[32, 20] G. Alberti,[42, 43] B. Alpat,[42] A. Alvino,[42, 43] G. Ambrosi,[42] K. Andeen,[28]
H. Anderhub,[54] L. Arruda,[30] P. Azzarello,[42, 21, *] A. Bachlechner,[1] F. Barao,[30] B. Baret,[22]
A. Barrau,[22] L. Barrin,[20] A. Bartoloni,[47] L. Basara,[5] A. Basili,[11] L. Batalha,[30] J. Bates,[25]
R. Battiston,[42, 43, 46] J. Bazo,[42] R. Becker,[11] U. Becker,[11] M. Behlmann,[11] B. Beischer,[1]
J. Berdugo,[32] P. Berges,[11] B. Bertucci,[42, 43] G. Bigongiari,[44, 45] A. Biland,[54] V. Bindi,[24]
S. Bizzaglia,[42] G. Boella,[36, 37] W. de Boer,[28] K. Bollweg,[25] J. Bolmont,[38] B. Borgia,[47, 48]
S. Borsini,[42, 43] M.J. Boschini,[36] G. Boudoul,[22] M. Bourquin,[21] P. Brun,[5] M. Buénerd,[22]
J. Burger,[11] W. Burger,[43] F. Cadoux,[5, 21] X.D. Cai,[11] M. Capell,[11] D. Casadei,[9, 10]
J. Casaus,[32] V. Cascioli,[42, 43] G. Castellini,[18] I. Cernuda,[32] F. Cervelli,[44] M.J. Chae,[49]
Y.H. Chang,[12] A.I. Chen,[11] C.R. Chen,[26] H. Chen,[11] G.M. Cheng,[8] H.S. Chen,[8]
L. Cheng,[50] N. Chernoplyiokov,[39] A. Chikanian,[41] E. Choumilov,[11] V. Choutko,[11]
C.H. Chung,[1] C. Clark,[25] R. Clavero,[29] G. Coignet,[5] V. Commichau,[54] C. Consolandi,[36, 24]
A. Contin,[9, 10] C. Corti,[24] M.T. Costado Dios,[29] B. Coste,[22] D. Crespo,[32] Z. Cui,[50] M. Dai,[7]
C. Delgado,[32] S. Della Torre,[36, 37] B. Demirkoz,[4] P. Dennett,[11] L. Derome,[22] S. Di Falco,[44]
X.H. Diao,[23] A. Diago,[29] L. Djambazov,[54] C. Díaz,[32] P. von Doetinchem,[1] W.J. Du,[50]
J.M. Dubois,[5] R. Duperay,[22] M. Duranti,[42, 43] D. D'Urso,[42, 20] A. Egorov,[11] A. Eline,[11]
F.J. Eppling,[11] T. Eronen,[53] J. van Es,[17] H. Esser,[1] A. Falvard,[38] E. Fiandrini,[42, 43]
A. Fiasson,[5] E. Finch,[41] P. Fisher,[11] K. Flood,[11] R. Foglio,[22] M. Fohey,[25] S. Fopp,[1]
N. Fouque,[5] Y. Galaktionov,[11] M. Gallilee,[11] L. Gallin-Martel,[22] G. Gallucci,[44] B. García,[32]
J. García,[32] R. García-López,[29] L. García-Tabares,[32] C. Gargiulo,[47, 11] H. Gast,[1]
I. Gebauer,[28] S. Gentile,[47, 48] M. Gervasi,[36, 37] W. Gillard,[22] F. Giovacchini,[32] L. Girard,[5]
P. Goglov,[11] J. Gong,[40] C. Goy-Henningsen,[5] D. Grandi,[36] M. Graziani,[42, 43] A. Grechko,[39]
A. Gross,[1] I. Guerri,[44, 45] C. de la Guía,[32] K.H. Guo,[23] M. Habiby,[21] S. Haino,[42, 12]
F. Hauler,[28] Z.H. He,[23] M. Heil,[28] J. Heilig,[25] R. Hermel,[5] H. Hofer,[54] Z.C. Huang,[23]
W. Hungerford,[11, 25] M. Incagli,[44, 11] M. Ionica,[42, 43] A. Jacholkowska,[38] W.Y. Jang,[16]
H. Jinchi,[31] M. Jongmanns,[54, †] L. Journet,[5] L. Jungermann,[28] W. Karpinski,[1] G.N. Kim,[16]
K.S. Kim,[16] Th. Kirn,[1] R. Kossakowski,[5] A. Koulemzine,[11] O. Kounina,[11] A. Kounine,[11]
V. Koutsenko,[11] M.S. Krafczyk,[11] E. Laudi,[42, 43, ‡] G. Laurenti,[9] C. Lauritzen,[25]
A. Lebedev,[11] M.W. Lee,[16] S.C. Lee,[52] C. Leluc,[21] H. León Vargas,[33] V. Lepareur,[5]
J.Q. Li,[40] Q. Li,[40] T.X. Li,[23] W. Li,[6] Z.H. Li,[8] P. Lipari,[47] C.H. Lin,[52] D. Liu,[52] H. Liu,[40]
T. Lomtadze,[44] Y.S. Lu,[8] S. Lucidi,[42] K. Lübelsmeyer,[1] J.Z. Luo,[40] W. Lustermann,[54]
S. Lv,[23] J. Madsen,[2] R. Majka,[41] A. Malinin,[14] C. Mañá,[32] J. Marín,[32] T. Martin,[25]
G. Martínez,[32] F. Masciocchi,[21] N. Masi,[9, 10] D. Maurin,[22] A. McInturff,[15] P. McIntyre,[15]
A. Menchaca-Rocha,[33] Q. Meng,[40] M. Menichelli,[42] I. Mereu,[42, 43] M. Millinger,[1] D.C. Mo,[23]
M. Molina,[§] P. Mott,[25] A. Mujunen,[27] S. Natale,[1, 52] P. Nemeth,[25] J.Q. Ni,[23] N. Nikonov,[28]
F. Nozzoli,[42, 19] P. Nunes,[30] A. Obermeier,[28] S. Oh,[49] A. Oliva,[42, 43, 32] F. Palmonari,[9, 10]
C. Palomares,[32] M. Paniccia,[5, 21] A. Papi,[42] W.H. Park,[16] M. Pauluzzi,[42, 43] F. Pauss,[54]
A. Pauw,[17] E. Pedreschi,[44] S. Pensotti,[36, 37] R. Pereira,[30] E. Perrin,[21] G. Pessina,[36, 37]
G. Pierschel,[1] F. Pilo,[44] A. Piluso,[42, 43] C. Pizzolotto,[42, 19] V. Plyaskin,[11] J. Pochon,[5, 29]

M. Pohl,[21] V. Poireau,[5] S. Porter,[25] J. Pouxe,[22] A. Putze,[1] L. Quadrani,[9, 10] X.N. Qi,[23]
P.G. Rancoita,[36] D. Rapin,[21] Z.L. Ren,[52] J.S. Ricol,[22] E. Riihonen,[53] I. Rodríguez,[32]
U. Roeser,[54] S. Rosier-Lees,[5] L. Rossi,[35, 20] A. Rozhkov,[11] D. Rozza,[36, 37, 20] A. Sabellek,[28]
R. Sagdeev,[13] J. Sandweiss,[41] B. Santos,[30] P. Saouter,[21] M. Sarchioni,[42] S. Schael,[1]
D. Schinzel,[11] M. Schmanau,[28] G. Schwering,[1] A. Schulz von Dratzig,[1] G. Scolieri,[42]
E.S. Seo,[14] B.S. Shan,[6] J.Y. Shi,[40] Y.M. Shi,[51] T. Siedenburg,[1] R. Siedling,[1] D. Son,[16]
F. Spada,[47] F. Spinella,[44] M. Steuer,[11] K. Stiff,[15] W. Sun,[11] W.H. Sun,[40] X.H. Sun,[23]
M. Tacconi,[36, 37] C.P. Tang,[23] X.W. Tang,[8] Z.C. Tang,[8] L. Tao,[5] J. Tassan-Viol,[5]
Samuel C.C. Ting,[11] S.M. Ting,[11] C. Titus,[11] N. Tomassetti,[42, 43] F. Toral,[32] J. Torsti,[53]
J.R. Tsai,[26] J.C. Tutt,[25] J. Ulbricht,[54] T. Urban,[25] V. Vagelli,[28] E. Valente,[47] C. Vannini,[44]
E. Valtonen,[53] M. Vargas Trevino,[22] S. Vaurynovich,[11] M. Vecchi,[12] M. Vergain,[11]
B. Verlaat,[3] C. Vescovi,[22] J.P. Vialle,[5] G. Viertel,[54] G. Volpini,[34, 35] D. Wang,[26] N.H. Wang,[50]
Q.L. Wang,[7] R.S. Wang,[51] X. Wang,[11] Z.X. Wang,[23] W. Wallraff,[1] Z.L. Weng,[23, 52]
M. Willenbrock,[11] M. Wlochal,[1] H. Wu,[40] K.Y. Wu,[6, 52] Z.S. Wu,[23] W.J. Xiao,[23] S. Xie,[51]
R.Q. Xiong,[40] G.M. Xin,[50] N.S. Xu,[23] W. Xu,[8] Q. Yan,[8] J. Yang,[49] M. Yang,[8] Q.H. Ye,[51]
H. Yi,[40] Y.J. Yu,[7] Z.Q. Yu,[8] S. Zeissler,[28] J.G. Zhang,[40] Z. Zhang,[23] M.M. Zhang,[23]
Z.M. Zheng,[6] H.L. Zhuang,[8] V. Zhukov,[1] A. Zichichi,[9, 10] P. Zuccon,[42, 11] and C. Zurbach[38]

(AMS Collaboration)

[1]*I. Physikalisches Institut B, RWTH, D–52056 Aachen, Germany*¶
[2]*Department of Physics and Astronomy, University
of Aarhus, DK–8000 Aarhus C, Denmark*
[3]*National Institute for Nuclear Physics and High Energy
Physics, NIKHEF, NL-1098 SJ Amsterdam, The Netherlands*
[4]*Department of Physics, Middle East Technical University, METU, 06800 Ankara, Turkey*
[5]*Laboratoire d'Annecy–Le–Vieux de Physique des Particules, LAPP,
IN2P3/CNRS and Université de Savoie, F–74941 Annecy–le–Vieux, France*
[6]*Beihang University, BUAA, Beijing, 100191, China*
[7]*Institute of Electrical Engineering, IEE, Chinese
Academy of Sciences, Beijing, 100080, China*
[8]*Institute of High Energy Physics, IHEP, Chinese
Academy of Sciences, Beijing, 100039, China*∗∗
[9]*INFN-Sezione di Bologna, AMSI-40126 Bologna, Italy*††
[10]*Università di Bologna, AMSI-40126 Bologna, Italy*
[11]*Massachusetts Institute of Technology, MIT, Cambridge, MA 02139, USA*
[12]*National Central University, NCU, Chung–Li, Tao Yuan 32054, Taiwan*
[13]*East–West Center for Space Science, University
of Maryland, College Park, MD 20742, USA*
[14]*IPST, University of Maryland, College Park, MD 20742, USA*
[15]*Department of Physics, Texas A&M University, College Station, TX 77843, USA*
[16]*CHEP, Kyungpook National University, 702–701 Daegu, Korea*
[17]*National Aerospace Laboratory, NLR, NL–8300 AD Emmeloord, the Netherlands*
[18]*CNR–IROE, AMSI-50125 Firenze, Italy*
[19]*ASDC ESRIN, AMSI-00044 Frascati, Italy*
[20]*European Organization for Nuclear Research, CERN, CH–1211 Geneva 23, Switzerland*
[21]*DPNC, Université de Genève, CH–1211 Genève 4, Switzerland*

[22]*Laboratoire de Physique subatomique et de cosmologie, LPSC, IN2P3/CNRS and Université Joseph Fourier, Grenoble INP, F–38026 Grenoble, France*

[23]*Sun Yat–sen University, SYSU, Guangzhou, 510275, China*

[24]*University of Hawaii, Physics and Astronomy Department, 2505 Correa Road, WAT 432; Honolulu, HI 96822, USA*

[25]*NASA, National Aeronautics and Space Administration, Johnson Space Center, JSC, and Jacobs-Sverdrup, Houston, TX 77058, USA*

[26]*National Space Organization, Hsin-Chu City, 300, Taiwan*

[27]*Metsahovi Radio Observatory, Helsinki University of Technology, FIN–02540 Kylmala, Finland*

[28]*Institut für Experimentelle Kernphysik, Karlsruhe Institute of Technology, KIT, D–76128 Karlsruhe, Germany*[¶]

[29]*Instituto de Astrofísica de Canarias, IAC, E–38205, La Laguna, Tenerife, Spain*

[30]*Laboratório de Instrumentação e Física Experimental de Partículas, LIP, P–1000 Lisboa, Portugal*

[31]*Chung–Shan Institute of Science and Technology, Lung–Tan, Tao Yuan 325, Taiwan*

[32]*Centro de Investigaciones Energéticas, Medioambientales y Tecnológicas, CIEMAT, E–28040 Madrid, Spain*[‡‡]

[33]*Instituto de Física, Universidad Nacional Autónoma de México, UNAM, México, D. F., 01000 México*

[34]*INFN-Sezione di Milano, AMSI-20090 Milano, Italy*

[35]*Università di Milano, AMSI-20090 Milano, Italy*

[36]*INFN-Sezione di Milano–Bicocca, AMSI-20126 Milano, Italy*[††]

[37]*Università di Milano–Bicocca, AMSI-20126 Milano, Italy*[††]

[38]*Laboratoire Univers et Particules de Montpellier, LUPM (ex LPTA), IN2P3/CNRS and Université de Montpellier II, F–34095 Montpellier, France*

[39]*Kurchatov Institute, Russian Research Centre, Moscow, 123182, Russia*

[40]*Southeast University, SEU, Nanjing, 210096, China*

[41]*Physics Department, Yale University, New Haven, CT 06520, USA*

[42]*INFN-Sezione di Perugia, AMSI-06100 Perugia, Italy*[††]

[43]*Università di Perugia, AMSI-06100 Perugia, Italy*[††]

[44]*INFN-Sezione di Pisa, AMSI-56100 Pisa, Italy*[††]

[45]*Università di Pisa, AMSI-56100 Pisa, Italy*[††]

[46]*INFN–TIFPA and Università di Trento, AMSI-38123 Povo, Trento, Italy*[††]

[47]*INFN-Sezione di Roma 1, AMSI-00185 Roma, Italy*[††]

[48]*Università di Roma La Sapienza, AMSI-00185 Roma, Italy*[††]

[49]*Department of Physics, Ewha Womans University, Seoul, 120-750, Korea*

[50]*Shandong University, SDU, Jinan, Shandong, 250100, China*

[51]*Shanghai Jiaotong University, SJTU, Shanghai, 200030, China*

[52]*Institute of Physics, Academia Sinica, Nankang, Taipei 11529, Taiwan*

[53]*Space Research Laboratory, Department of Physics, University of Turku, FIN–20014 Turku, Finland*

[54]*Institute for Particle Physics, ETH Zürich, CH–8093 Zürich, Switzerland*

(Dated: March 15, 2013)

Abstract

A precision measurement by AMS on the ISS of the positron fraction in primary cosmic rays in the energy range from 0.5 to 350 GeV based on 6.8 million positron and electron events is presented. The very accurate data show that the positron fraction is steadily increasing from 10 to $\sim$250 GeV, but, from 20 to 250 GeV, the slope decreases by an order of magnitude. The positron fraction spectrum shows no fine structure and the positron to electron ratio shows no observable anisotropy. Together, these features show the existence of new physical phenomena.

Introduction. The Alpha Magnetic Spectrometer, AMS-02, is a general purpose high energy particle physics detector. It was installed on the International Space Station, ISS, on 19 May 2011 to conduct a unique long duration mission ($\sim$20 years) of fundamental physics research in space. The first AMS results reported in this article are based on the data collected during the initial 18 months of operations on the ISS, from 19 May 2011 to 10 December 2012. This constitutes 8% of the expected AMS data sample. The positron fraction, that is, the ratio of the positron flux to the combined flux of positrons and electrons, is presented in this report in the energy range from 0.5 to 350 GeV. Over the last 2 decades, there has been strong interest in the cosmic ray positron fraction in both particle physics and astrophysics [1]. The purpose of this paper is to present the accurate determination of this fraction as a function of energy and direction (anisotropy).

AMS detector. The layout of the AMS-02 detector [2] is shown in Figure 1. It consists of 9 planes of precision silicon Tracker; a Transition Radiation Detector, TRD; four planes of Time of Flight counters, TOF; a permanent Magnet; an array of anti-coincidence counters, ACC, surrounding the inner Tracker; a Ring Imaging Čerenkov detector, RICH; and an Electromagnetic Calorimeter, ECAL. The figure also shows a high energy positron of 369 GeV recorded by AMS.

The AMS coordinate system is concentric with the center of the Magnet. The x-axis is parallel to the main component of the magnetic field and the z-axis points vertically. The (y–z) plane is the bending plane. AMS is mounted on the ISS with a 12° roll to port to avoid the ISS solar panels being in the detector field of view; terms such as "above", "below" and "downward-going" refer to the AMS coordinate system.

The Tracker accurately determines the trajectory and absolute charge (Z) of cosmic rays by multiple measurements of the coordinates and energy loss. It is composed of 192 ladders, each containing double-sided silicon sensors, readout electronics and mechanical support [3, 4]. Three planes of aluminum honeycomb with carbon fiber skins are equipped with ladders on both sides of the plane. These double planes are numbered 3 to 8, see Figure 1. Another three planes are equipped with one layer of silicon ladders. As indicated in Figure 1, plane 1 is located on top of the TRD, plane 2 is above the Magnet and plane 9 is between the RICH and the ECAL. Plane 9 covers the ECAL acceptance. Planes 2 through 8 constitute the inner Tracker. Coordinate resolution of each plane is measured to be better than $10\,\mu$m in the bending direction and the charge resolution is $\Delta Z \simeq 0.06$ at $Z = 1$. The total lever arm of the Tracker from plane 1 to plane 9 is 3.0 m. Positions of the planes of the inner Tracker are held stable by a special carbon fiber structure [5]. It is monitored using 20 IR laser beams which penetrate through all planes of the inner Tracker and provide micron level accuracy position measurements. The positions of planes 1 and 9 are aligned using cosmic ray protons such that they are stable to $3\,\mu$m (see Figure 2).

The TRD is designed to use transition radiation to distinguish between e$^{\pm}$ and protons, and dE/dx to independently identify nuclei [6]. It consists of 5,248 proportional tubes of 6 mm diameter with a maximum length of 2 m arranged side-by-side in 16-tube modules. The 328 modules are mounted in 20 layers. Each layer is interleaved with a 20 mm thick fiber fleece radiator, LRP375, with a density of $0.06\,\text{g/cm}^3$. There are twelve layers of proportional tubes along the y-axis located in the middle of the TRD and, along the x-axis, four layers located on top and four on the bottom. The tubes are filled with a 90:10 Xe:CO_2 mixture. Experience over the first 18 months of operations on the ISS shows, as expected, a very small, diffusion dominated leak rate. The onboard gas supplies contained, at launch, 49 kg of Xe and 5 kg of CO_2 which ensures $\sim$30 years of steady TRD operations in space. In order

to differentiate between e$^\pm$ and protons, signals from the 20 layers are combined in a TRD estimator formed from the ratio of the log–likelihood probability of the e$^\pm$ hypothesis to that of the proton hypothesis. Positrons and electrons have a TRD estimator value $\sim$0.5 and protons $\sim$1. This allows the efficient discrimination of the proton background.

Two planes of TOF counters are located above and two planes below the Magnet [7]. Each plane contains 8 or 10 scintillating paddles. Each paddle is equipped with 2 or 3 PMTs on each end for efficient detection of traversing particles. The coincidence of signals from all four planes provides a charged particle trigger. The TOF charge resolution, obtained from multiple measurements of the ionization energy loss, is $\Delta Z \simeq 0.05$ at $Z = 1$. The average time resolution of each counter has been measured to be 160 picoseconds and the overall velocity ($\beta = v/c$) resolution of the system has been measured to be 4 % for $\beta \simeq 1$ and $Z = 1$ particles, which also discriminates between upward- and downward-going particles. The timing resolution improves with increasing magnitude of the charge to a limit of $\Delta t \sim 50$ ps and $\Delta\beta/\beta \sim 1$ % for $Z > 5$ particles.

The Magnet [4, 5] is made of 64 high-grade Nd-Fe-B sectors assembled in a cylindrical shell structure 0.8 m long with an inner diameter of 1.1 m. This configuration produces a field of 1.4 kG in the x direction at the center of the magnet and negligible dipole moment outside the magnet. This is important in order to eliminate the effect of torque on the Space Station. The detailed 3-dimensional field of the Magnet was mapped in 2010. The field was measured in 120,000 locations to an accuracy of better than 1 %. Comparison with the measurements performed with the same Magnet in 1997, before the engineering flight of AMS-01, shows that the field did not change within 1 %, limited by the accuracy of the 1997 measurement. Together with the Tracker, the Magnet provides a Maximum Detectable Rigidity of 2 TV on average, over Tracker planes 1 to 9, where rigidity is the momentum divided by the charge.

The ACC counters surround the inner Tracker inside the Magnet bore [8]. Their purpose is to detect events with unwanted particles that enter or leave the inner Tracker volume transversely. The ACC consists of sixteen curved scintillator panels of 0.8 m length, instrumented with wavelength shifting fibers to collect the light. To maintain the hermeticity of the ACC cylinder, the counters have a tongue and a groove along the vertical edges such that particles crossing this area are detected simultaneously by two panels. Long duration tests of the counters show they have an efficiency close to 0.99999.

The RICH is designed to measure the magnitude of the charge of cosmic rays and their velocities with a precision of $\Delta\beta/\beta \sim 1/1000$ [9]. It consists of two non-overlapping dielectric radiators, one in the center with a refractive index of $n = 1.33$, corresponding to a Čerenkov threshold of $\beta > 0.75$, surrounded by a radiator with $n = 1.05$, with a threshold of $\beta > 0.95$. The Čerenkov photons are detected by an array of 10,880 photosensors with an effective spatial granularity of 8.5$\times$8.5 mm^2 at an expansion distance of 45 cm. To reduce lateral losses, the expansion volume is surrounded by a high reflectivity mirror with the shape of a truncated cone.

The ECAL consists of a multilayer sandwich of 98 lead foils and $\sim$50,000 scintillating fibers with an active area of 648$\times$648 mm^2 and a thickness of 166.5 mm corresponding to 17 radiation lengths [10]. The calorimeter is composed of 9 superlayers, each 18.5 mm thick and made of 11 grooved, 1 mm thick lead foils interleaved with 10 layers of 1 mm diameter scintillating fibers (the last foil of the last superlayer is made of aluminum). In each superlayer, the fibers run in one direction only. The 3–D imaging capability of the detector is obtained by stacking alternate superlayers with fibers parallel to the x- and

y-axes (5 and 4 superlayers, respectively). The fibers are read out on one end by 1,296 photosensors with a linearity of $1/10^5$ per sensor. From the beam tests of the complete AMS detector, the energy resolution of the ECAL is parametrized as a function of energy (in GeV) $\sigma(E)/E = \sqrt{(0.104)^2/E + (0.014)^2}$. In order to cleanly identify electrons and positrons, an ECAL estimator, based on a Boosted Decision Tree, BDT, algorithm [11], is constructed using the 3–D shower shape in the ECAL.

The AMS electronics consists of 650 microprocessors and ~300,000 readout channels. All components and circuits used in the electronics passed rigorous selection and space qualification tests [2]. The tests include irradiation with heavy ions at GSI, Germany and Catania, Italy and protons in Indiana, USA and at the SPS, CERN. Thermal and thermal-vacuum tests were performed at CSIST, Taiwan and SERMS, Terni, Italy. Onboard data processing reduces the raw data volume by a factor of 1,000 without the loss of physics information. The collected data are downlinked to the ground at an average rate of 10 Mbit/s. On the ISS, the particle rates in the acceptance vary from 200 Hz near the Equator to about 2,000 Hz near the Earth's magnetic poles. The data acquisition efficiency is 86 % on average resulting in an average event acquisition rate of ~600 Hz.

The thermal environment on the ISS is constantly changing. To ensure that components operate within their non-destructive thermal limits, AMS is equipped with 1,118 temperature sensors, five radiators and 298 thermostatically controlled heaters. The Tracker Thermal Control System [12], TTCS, keeps the Tracker frontend electronics temperatures stable within 1°C to ensure its optimal performance (see Figure 2a).

There are three main detectors that allow a significant reduction of the proton background in the identification of the positron and electron samples. These are the TRD (above the Magnet), the ECAL (below the Magnet) and the Tracker. The TRD and the ECAL are separated by the Magnet and the Tracker. This ensures that secondary particles produced in the TRD and the upper TOF planes are swept away and do not enter into the ECAL. Events with large angle scattering are also rejected by a quality cut on the measurement of the trajectory using the Tracker. The matching of the ECAL energy and the momentum measured with the Tracker greatly improves the proton rejection. The proton rejection power of the TRD estimator at 90 % $e^{\pm}$ efficiency measured on orbit is 10^3 to 10^4, as shown in [13]. The proton rejection power of the ECAL estimator when combined with the energy-momentum matching requirement $E/p > 0.75$ (see [13]) reaches ~10,000. The performance of both the TRD and ECAL estimators are derived from data taken on the ISS. Note that the proton rejection power can be readily improved by tightening the selection criteria with reduced $e^{\pm}$ efficiency.

The complete AMS detector was tested in thermal–vacuum and electromagnetic interference chambers at the European Space Agency test facility (ESTEC) in the Netherlands. The complete detector was also tested at the SPS at CERN, both before and after the ESTEC tests. These tests show that the detector functions as designed. In the beam tests, AMS was exposed to secondary beams of positrons and electrons in the momentum range from 10 to 290 GeV/c and the primary 400 GeV/c proton beam. It was also exposed to 10 to 180 GeV/c charged pions which produce transition radiation as protons up to 1.2 TeV/c. The test beams were injected not only over the full acceptance above the detector, but also from the bottom and the sides, to simulate the arrival of cosmic rays at AMS on the ISS. These data have a crucial role in the analysis, especially in the definition of the absolute energy scale of the ECAL and the rigidity scale of the Tracker. The benchmark performance of AMS, met during the beam tests at CERN, is an $e^{\pm}$ to proton separation of 10^6

at $400\,\text{GeV/c}$.

Data sample and analysis procedure. Over 25 billion events have been analyzed. Optimization of all reconstruction algorithms was performed using the test beam data. Corrections are applied to the data to ensure long term stability of the absolute scales in the varying on orbit environment. These corrections are determined using specific samples of particles, predominantly protons. In addition, stability of the electronics response is ensured by calibrations of all channels every half-orbit ($\sim$46 min).

Monte Carlo simulated events are produced using a dedicated program developed by AMS which is based on the GEANT-4.9.4 package [14]. This program simulates electromagnetic and hadronic interactions of particles in the materials of AMS and generates detector responses. The digitization of the signals, including those of the AMS trigger, is simulated precisely according to the measured characteristics of the electronics. The digitized signals then undergo the same reconstruction as used for the data. The Monte Carlo samples used in the present analysis have sufficient statistics such that they do not contribute to the errors.

For this analysis, events are selected by requiring a track in the TRD and in the Tracker, a cluster of hits in the ECAL and a measured velocity $\beta \sim 1$ in the TOF consistent with a downward-going $Z = 1$ particle. In order to reject $> 99\,\%$ of the remaining protons, an energy-dependent cut on the ECAL estimator is applied. In order to reject positrons and electrons produced by the interaction of primary cosmic rays with the atmosphere [15], the energy measured with the ECAL is required to exceed by a factor of 1.2 the maximal Stoermer cutoff [16] for either a positive or a negative particle at the geomagnetic location where the particle was detected and at any angle within the AMS acceptance.

The overall selection efficiency for positrons and electrons is estimated to be $\sim$90$\,\%$ in the acceptance of the ECAL. Any charge asymmetry in the selection efficiency, important only at very low energies (below $3\,\text{GeV}$), is accounted for in the systematics. The remaining sample contains $\sim$6,800,000 primary positrons and electrons and $\sim$700,000 protons. The composition of the sample versus energy is determined by the TRD estimator and E/p matching.

The positron fraction is determined in ECAL energy bins. The binning is chosen according to the energy resolution and the available statistics such that migration of the signal events to neighboring bins has a negligible contribution to the systematic errors above $\sim$2$\,\text{GeV}$. The migration uncertainty was obtained by folding the measured rates of positrons and electrons with the ECAL energy resolution.

In every energy bin, the 2-dimensional reference spectra for e$^{\pm}$ and the background are fitted to data in the (TRD estimator–$\log(E/p)$) plane by varying the normalizations of the signal and the background. This method provides a data driven control of the dominant systematic uncertainties by combining the redundant TRD, ECAL and Tracker information. The reference spectra are determined from high statistics, clean electron and proton data samples selected using ECAL information and their Monte Carlo simulation. The 2–D positron reference spectra were verified to be equal to the electron reference spectra using the test beam data. The proton reference spectra are selected using the ECAL estimator. The fit is performed for positive and negative rigidity data samples yielding, respectively, the numbers of positrons and electrons. Results of a fit for the positive sample in the range 83.2–$100\,\text{GeV}$ are presented in Figure 3 as a projection onto the TRD estimator axis, where the noted charge confusion contribution is from electrons misidentified as positrons.

There are several sources of systematic uncertainty including those associated with the

asymmetric acceptance of e^+ and e^-, the selection of $e^\pm$, bin-to-bin migration, the reference spectra and charge confusion.

Two sources of charge confusion dominate. The first is related to the finite resolution of the Tracker and multiple scattering. It is mitigated by the E/p matching and the quality cut of the trajectory measurement. The second source is related to the production of secondary tracks along the path of the primary $e^\pm$ in the Tracker. The impact of the second effect was estimated using control data samples of electron events with the ionization in the lower TOF counters corresponding to at least two traversing particles. Both sources of charge confusion are found to be well reproduced by the Monte Carlo simulation. The systematic uncertainties due to these two effects are obtained by varying the background normalizations within the statistical limits. As an example, for the positive sample in the range 83.2–100 GeV the uncertainty on the number of positrons due to the charge confusion is 1.0 %.

The systematic uncertainties were examined in each energy bin over the entire spectrum from 0.5 to 350 GeV.

As seen in Figure 3, the proton contamination in the region populated by positrons is small, $\sim$1 % in this energy range. It is accurately measured using the TRD estimator and therefore has a negligible contribution to the overall error. The systematic error associated with the uncertainty of the reference spectra arises from their finite statistics. It is measured by varying the shape of the reference spectra within the statistical uncertainties. Its contribution to the overall error is small compared to the statistics and is included in the total systematic error.

To evaluate systematic uncertainties related to the selection, the complete analysis is repeated in every energy bin $\sim$1,000 times with different cut values, such that the selection efficiency varies by 20–30 %. Figure 4a shows the resulting variation of the positron fraction over a range of 83.2-100 GeV. The difference between the width of this distribution from data and from Monte Carlo quantifies the systematic uncertainty due to the selection. Figure 4b shows no correlation between the measured positron fraction and the number of selected positrons.

Results and conclusions. The measured positron fraction is presented in Figure 5 as a function of the reconstructed energy at the top of the AMS detector and Table 1 shows the values for a few representative energy bins (for the complete table, see [13]). As seen in the figure, below 10 GeV the positron fraction decreases with increasing energy as expected from the secondary production of cosmic rays by collision with the interstellar medium. The positron fraction is steadily increasing from 10 to $\sim$250 GeV. This is not consistent with only the secondary production of positrons [17]. The behavior above 250 GeV will become more transparent with more statistics which will also allow improved treatment of the systematics.

Table 1 (see also [13]) also presents the contribution of individual sources to the systematic error for different bins which are added in quadrature to arrive at the total systematic uncertainty. As seen, the total systematic error at the highest energies is dominated by the uncertainty in the magnitude of the charge confusion.

Most importantly, several independent analyses were performed on the same data sample by different study groups. Results of these analyses are consistent with those presented in Figure 5 and in Table 1 (see also [13]).

The observation of the positron fraction increase with energy has been reported by earlier experiments: TS93 [18], Wizard/CAPRICE [19], HEAT [20], AMS-01 [21], PAMELA [22] and Fermi-LAT [23]. The most recent results are presented in Figure 5 for comparison. The accuracy of AMS-02 and high statistics available enable the reported AMS-02 positron frac-

9

tion spectrum to be clearly distinct from earlier work. The AMS-02 spectrum has the unique resolution, statistics and energy range to provide accurate information on new phenomena.

The accuracy of the data (Table 1 and [13]) enables us to investigate the properties of the positron fraction with different models. We present here the results of comparing our data with a minimal model, as an example. In this model the e^+ and e^- fluxes, Φ_{e^+} and Φ_{e^-}, are parametrized as the sum of individual diffuse power law spectra and the contribution of a single common source of $e^\pm$:

$$\Phi_{e^+} = C_{e^+} E^{-\gamma_{e^+}} + C_s E^{-\gamma_s} e^{-E/E_s}; \tag{1}$$

$$\Phi_{e^-} = C_{e^-} E^{-\gamma_{e^-}} + C_s E^{-\gamma_s} e^{-E/E_s}, \tag{2}$$

(with E in GeV) where the coefficients C_{e^+} and C_{e^-} correspond to relative weights of diffuse spectra for positrons and electrons and C_s to the weight of the source spectrum; γ_{e^+}, γ_{e^-} and γ_s are the corresponding spectral indexes; and E_s is a characteristic cutoff energy for the source spectrum. With this parametrization the positron fraction depends on 5 parameters. A fit to the data in the energy range 1 to 350 GeV based on the number of events in each bin yields a $\chi^2/d.f. = 28.5/57$ and

$\gamma_{e^-} - \gamma_{e^+} = -0.63 \pm 0.03$, *i.e.*, the diffuse positron spectrum is softer, that is, less energetic with increasing energy, than the diffuse electron spectrum;

$\gamma_{e^-} - \gamma_s = 0.66 \pm 0.05$, *i.e.*, the source spectrum is harder than the diffuse electron spectrum;

$C_{e^+}/C_{e^-} = 0.091 \pm 0.001$, *i.e.*, the weight of the diffuse positron flux amounts to $\sim 10\%$ of that of the diffuse electron flux;

$C_s/C_{e^-} = 0.0078 \pm 0.0012$, *i.e.*, the weight of the common source constitutes only $\sim 1\%$ of that of the diffuse electron flux;

$1/E_s = 0.0013 \pm 0.0007\,\text{GeV}^{-1}$, corresponding to a cutoff energy of $760^{+1,000}_{-280}\,\text{GeV}$.

The fit is shown in Figure 6 as a solid curve. The agreement between the data and the model shows that the positron fraction spectrum is consistent with $e^\pm$ fluxes each of which is the sum of its diffuse spectrum and a single common power law source. No fine structures are observed in the data. The excellent agreement of this model with the data indicates that the model is insensitive to solar modulation effects [24] during this period. Indeed, fitting over the energy ranges from 0.8–350 GeV to 6.0–350 GeV does not change the results nor the fit quality. Furthermore, fitting the data with the same model extended to include different solar modulation effects on positrons and electrons yields similar results. This study also shows that the slope of the positron fraction as a function of energy decreases by an order of magnitude from 20 to 250 GeV.

Primary sources of cosmic ray positrons and electrons may induce some degree of anisotropy of the measured positron to electron ratio, that is, the ratio of the positron flux to the electron flux. Therefore, a systematic search for anisotropies using the selected sample is performed from 16 to 350 GeV.

Arrival directions of electrons and positrons are used to build a sky map in galactic coordinates, (b, l), containing the number of observed positrons and electrons. The fluctuations

of the observed positron ratio are described using a spherical harmonic expansion

$$\frac{r_{\rm e}(b,l)}{< r_{\rm e} >} - 1 = \sum_{\ell=0}^{\infty} \sum_{m=-\ell}^{\ell} a_{\ell m} \, Y_{\ell m}(\pi/2 - b, l), \tag{3}$$

where $r_{\rm e}(b,l)$ denotes the positron ratio at (b,l); $< r_{\rm e} >$ is the average ratio over the sky map; $Y_{\ell m}$ are spherical harmonic functions and $a_{\ell m}$ are the corresponding weights. The coefficients of the angular power spectrum of the fluctuations are defined as

$$C_\ell = \frac{1}{2\ell+1} \sum_{m=-\ell}^{\ell} |a_{\ell m}|^2. \tag{4}$$

They are found to be consistent with the expectations for isotropy at all energies and upper limits to multipole contributions are obtained. We obtain a limit on the amplitude of dipole anisotropy on the positron to electron ratio, $\delta = 3\sqrt{C_1/4\pi}$, for any axis in galactic coordinates of $\delta \le 0.036$ at the 95 % confidence level.

In conclusion, the first 6.8 million primary positron and electron events collected with AMS on the ISS show:

i. At energies $< 10\,\mathrm{GeV}$, a decrease in the positron fraction with increasing energy.

ii. A steady increase in the positron fraction from 10 to $\sim$250 GeV.

iii. The determination of the behavior of the positron fraction from 250 to 350 GeV and beyond requires more statistics.

iv. The slope of the positron fraction versus energy decreases by an order of magnitude from 20 to 250 GeV and no fine structure is observed. The agreement between the data and the model shows that the positron fraction spectrum is consistent with $e^{\pm}$ fluxes each of which is the sum of its diffuse spectrum and a single common power law source.

v. The positron to electron ratio is consistent with isotropy; $\delta \le 0.036$ at the 95 % confidence level.

These observations show the existence of new physical phenomena, whether from a particle physics or an astrophysical origin.

---

[*] Currently at ISDC, CH–1290 Versoix, Switzerland.

[†] Deceased.

[‡] Currently at OHB, D–28359 Bremen, Germany.

[§] Currently at Selex ES, I–20014 Nerviano MI, Italy.

[¶] Supported by the Deutsches Zentrum für Luft– und Raumfahrt, DLR.

[**] Supported by the National Natural Science Foundation of China.

[††] Also supported by the Italian Space Agency, ASI.

[‡‡] Also supported by SEIDI and CPAN.

[1] M. Turner and F. Wilczek, Phys. Rev. **D42** (1990) 1001;
J. Ellis, 26th ICRC Salt Lake City (1999) astro-ph/9911440;
H. Cheng, J. Feng and K. Matchev, Phys. Rev. Lett. **89** (2002) 211301;
S. Profumo and P. Ullio, J. Cosmology Astroparticle Phys. JCAP**07** (2004) 006;
D. Hooper and J. Silk, Phys. Rev. D **71** (2005) 083503;
E. Ponton and L. Randall, JHEP **0904** (2009) 080;
G. Kane, R. Lu and S. Watson, Phys. Lett. **B681** (2009) 151;
D. Hooper, P. Blasi and P. D. Serpico, JCAP 0901 **025** (2009) 0810.1527;
Y–Z. Fan *et al.*, Int. J. Mod. Phys. **D19** (2010) 2011;
M. Pato, M. Lattanzi and G. Bertone, JCAP **1012** (2010) 020.

[2] A. Kounine, Int. J. Mod. Phys. **E 21** (2012) 123005;
Samuel C.C. Ting, Proc. of 4th Intl. Conf. Particle and Fundamental Physics in Space, Geneva, 5–7 Nov. 2012, NUPHBP, to be published;

S.–C. Lee, Proc. 20th Intl. Conf. Supersymmetry and Unification of Fundamental Interactions (SUSY 2012), 13–18 Aug. 2012, Beijing, China, to be published;

M. Aguilar, Proc. XL Intl. Meet. on Fundamental Physics, Centro de Ciencias de Benasque Pedro Pascual, 29 May 2012, to be published;

S. Schael, Proc. 10th Symp. Sources and Detection of Dark Matter and Dark Energy in the Universe, Los Angeles, 22–24 Feb. 2012, to be published;

B. Bertucci, PoS, **EPS-HEP** (2011) 67;

M. Incagli, AIP Conf. Proc. **1223**, (2009) 43;

R. Battiston, Nucl. Instrum. Meth. **A 588** (2008) 227-234.

[3] B. Alpat *et al.*, Nucl. Instrum. Meth. **A 613** (2010) 207.

[4] K. Luebelsmeyer *et al.*, Nucl. Instrum. Meth. **A 654** (2011) 639.

[5] M. Aguilar *et al.*, Phys. Rep. **366/6** (2002) 331.

[6] Th. Kirn, Nucl. Instrum. Meth. **A 706C** (2013) 43;
Ph. Doetinchem *et al.*, Nucl. Instrum. Meth. **A 558** (2006) 526;
F. Hauler *et al.*, IEEE Trans. Nucl. Sci. **51** (2004) 1365.

[7] A. Basili *et al.*, Nucl. Instrum. Meth. **A 707** (2012) 99;
V. Bindi *et al.*, Nucl. Instrum. Meth. **A 623** (2010) 968.

[8] Ph. Doetinchem *et al.*, Nucl. Phys. **B 197** (2009) 15.

[9] M. Aguilar-Benitez *et al.*, Nucl. Instrum. Meth. **A 614** (2010) 237;
M. Aguilar-Benitez *et al.*, Proc. 30th ICRC (2007);
P. Aguayo *et al.*, Nucl. Instrum. Meth. **A 560** (2006) 291;
B. Baret *et al.*, Nucl. Instrum. Meth. **A 525** (2004) 126;
J. Casaus, Nucl. Phys. B (Proc. Suppl.) **113** (2002) 147.

[10] C. Adloff *et al.*, Nucl. Instrum. Meth. *accepted for publication 2013*;
S. Rosier-Lees *et al.*, J. of Physics: Conf. Series (JPCS), **404** (012034), Calor2012, 4–8 June 2012, Santa Fe, USA;
F. Cadoux *et al.*, Nucl. Phys. B (Proc. Suppl.) **113** (2002) 159.

[11] B. Roe *et al.*, Nucl. Instrum. Meth. **A 543** (2005) 577.

[12] G. Alberti *et al.*, Nucl. Instrum. Meth. *submitted* 2013.

[13] The supplemental material includes plots of the proton rejection power of the TRD estimator and of the ECAL estimator combined with $E/p > 0.75$ matching vs. energy, the main event selection cuts, a typical E/p distribution as well as the complete tabulation of the positron fraction vs. energy.

[14] J. Allison *et al.*, IEEE Trans. Nucl. Sci. **53** (2006) 270;
S. Agostinelli *et al.*, Nucl. Instrum. Meth. **A 506** (2003) 250.

[15] J. Alcaraz *et al.*, Phys. Lett. **B 484** (2000) 10; see also [5].

[16] C. Stoermer, The Polar Aurora, Oxford University Press, London (1950).

[17] P.D. Serpico, Astropart. Phys. **39-40** (2012) 2;
T. Delahaye *et al.*, Astron. Astrophys. **501** (2009) 821;
I. Moskalenko and A. Strong, Astrophys. J. **493** (1998) 693.
We have not included the model predictions as their uncertainty, $\mathcal{O}(20\%)$, is larger than our errors. We thank Dr. Moskalenko for useful discussions on this subject.

[18] R. Golden *et al.*, Astrophys. J. **457** (1996) L103.

[19] M. Boezio *et al.*, Adv. Sp. Res. **27-4** (2001) 669.

[20] J. J. Beatty *et al.*, Phys. Rev. Lett. **93** (2004) 241102;
M. A. DuVernois *et al.*, Astrophys. J. **559** (2001) 296.

[21] M. Aguilar *et al.*, Phys. Lett. **B 646** (2007) 145.

[22] P. Picozza, "Understanding Cosmic Rays with Balloon and Space Experiments", Proceedings of the 4th International Conference on Particle and Fundamental Physics in Space, Geneva, 5-7 Nov. 2012, NUPHBP, to be published. The value in the highest energy bin is the 90 % *C.L.* lower limit. We are grateful to Professor Picozza for providing us with accurate information on the PAMELA experiment. Note: 1) The data are obtained directly from the absolute fluxes of electrons and positrons, gotten independently. 2) The reported errors contain not only statistical errors, but also a portion of the systematics. 3) The data shown have been collected between June 2006 and January 2010. They represent an average of the solar modulation.
O. Adriani *et al.*, Astropart. Phys. **34** (2010) 1;
O. Adriani *et al.*, Nature **458** (2009) 607.

[23] M. Ackermann *et al.*, Phys. Rev. Lett. **108** (2012) 011103.

[24] I. Usoskin *et al.*, J. Geophysical Research **116** (2011) A02104;
Y. Asaoka *et al.*, Phys. Rev. Lett. **88-5** (2002) 051101-1.

TABLE I. Representative bins of the positron fraction as a function of energy. Errors due to: *stat.* statistical error, *acc.* acceptance asymmetry, *sel.* event selection, *mig.* bin-to-bin migration, *ref.* reference spectra, *c.c.* charge confusion and *syst.* total systematic error. For the complete table see [13].

| **Energy**[GeV]	**N_{e^+}**	**Fraction**	$\boldsymbol{\sigma_{stat.}}$	$\sigma_{acc.}$	$\sigma_{sel.}$	$\sigma_{mig.}$	$\sigma_{ref.}$	$\sigma_{c.c.}$	$\boldsymbol{\sigma_{syst.}}$
1.00 - 1.21	9,335	0.0842	0.0008	0.0005	0.0009	0.0008	0.0001	0.0005	0.0014
1.97 - 2.28	23,893	0.0642	0.0004	0.0002	0.0005	0.0002	0.0001	0.0002	0.0006
3.30 - 3.70	20,707	0.0550	0.0004	0.0001	0.0003	0.0000	0.0001	0.0002	0.0004
6.56 - 7.16	13,153	0.0510	0.0004	0.0001	0.0000	0.0000	0.0001	0.0002	0.0002
9.95 - 10.73	7,161	0.0519	0.0006	0.0001	0.0000	0.0000	0.0001	0.0002	0.0002
19.37 - 20.54	2,322	0.0634	0.0013	0.0001	0.0001	0.0000	0.0001	0.0002	0.0003
30.45 - 32.10	1,094	0.0701	0.0022	0.0001	0.0002	0.0000	0.0001	0.0003	0.0004
40.00 - 43.39	976	0.0802	0.0026	0.0002	0.0005	0.0000	0.0001	0.0004	0.0007
50.87 - 54.98	605	0.0891	0.0038	0.0002	0.0006	0.0000	0.0001	0.0004	0.0008
64.03 - 69.00	392	0.0978	0.0050	0.0002	0.0010	0.0000	0.0002	0.0007	0.0013
74.30 - 80.00	276	0.0985	0.0062	0.0002	0.0010	0.0000	0.0002	0.0010	0.0014
86.00 - 92.50	240	0.1120	0.0075	0.0002	0.0010	0.0000	0.0003	0.0011	0.0015
100.0 - 115.1	304	0.1118	0.0066	0.0002	0.0015	0.0000	0.0003	0.0015	0.0022
115.1 - 132.1	223	0.1142	0.0080	0.0002	0.0019	0.0000	0.0004	0.0019	0.0027
132.1 - 151.5	156	0.1215	0.0100	0.0002	0.0021	0.0000	0.0005	0.0024	0.0032
151.5 - 173.5	144	0.1364	0.0121	0.0002	0.0026	0.0000	0.0006	0.0045	0.0052
173.5 - 206.0	134	0.1485	0.0133	0.0002	0.0031	0.0000	0.0009	0.0050	0.0060
206.0 - 260.0	101	0.1530	0.0160	0.0003	0.0031	0.0000	0.0013	0.0095	0.0101
260.0 - 350.0	72	0.1550	0.0200	0.0003	0.0056	0.0000	0.0018	0.0140	0.0152
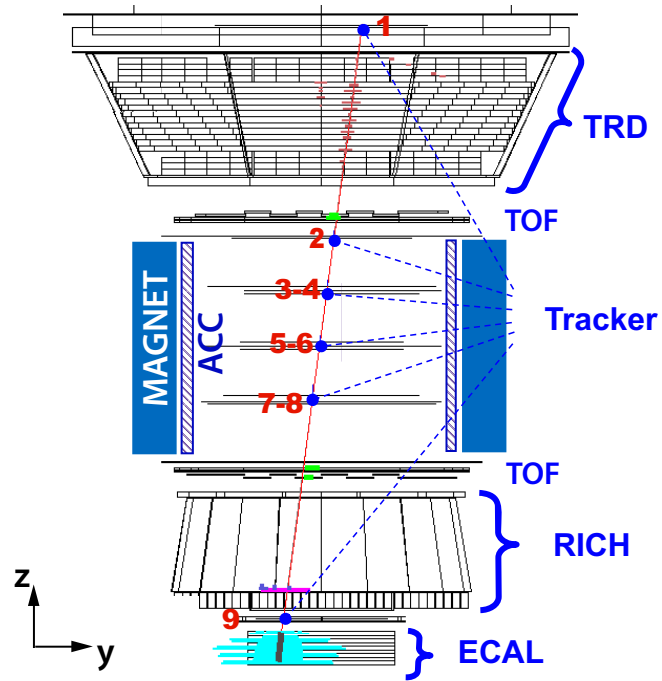
FIG. 1. A 369 GeV positron event as measured by the AMS detector on the ISS in the bending (y-z) plane. Tracker planes 1 to 9 measure the particle charge and momentum. The TRD identifies the particle as an electron. The TOF measures the charge and ensures that the particle is downward-going. The RICH independently measures the charge and velocity. The ECAL measures the 3–D shower profile, independently identifies the particle as an electron and measures its energy. An electron is identified by 1) an electron signal in the TRD, 2) an electron signal in the ECAL and 3) the matching of the ECAL shower energy and the momentum measured with the Tracker and Magnet.
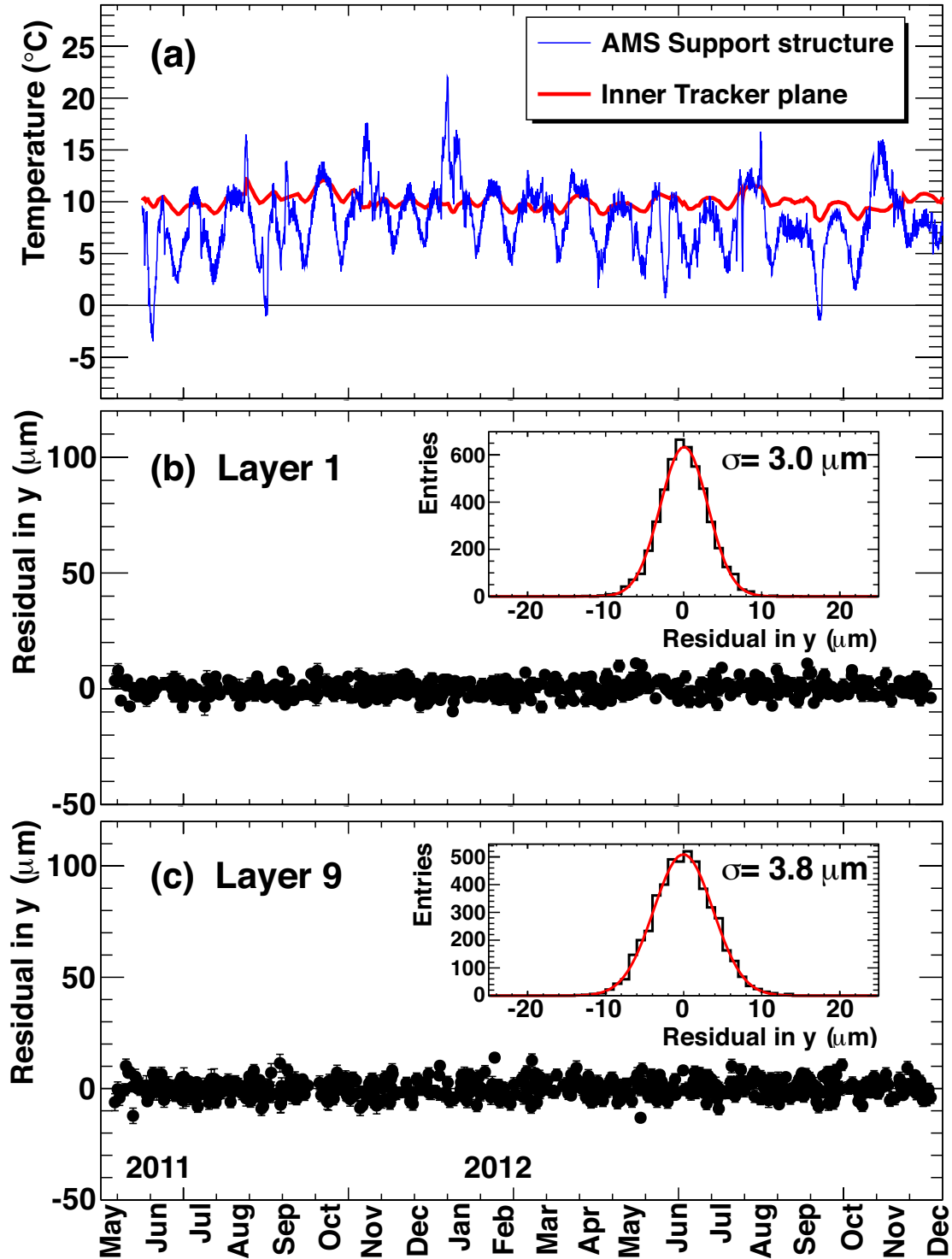
FIG. 2. Stability of the alignment of Tracker planes over more than 18 months of operation. (a) The temperature of the AMS support structure varies by 25°C, whereas the temperature of the inner Tracker planes remains within 1°C. As shown in (b), (c) and their inserts, the position of the outer planes 1 and 9, respectively, aligned using cosmic ray protons results in the precise tracing of their thermal movement over more than 18 months to a stability of $3\,\mu$m.
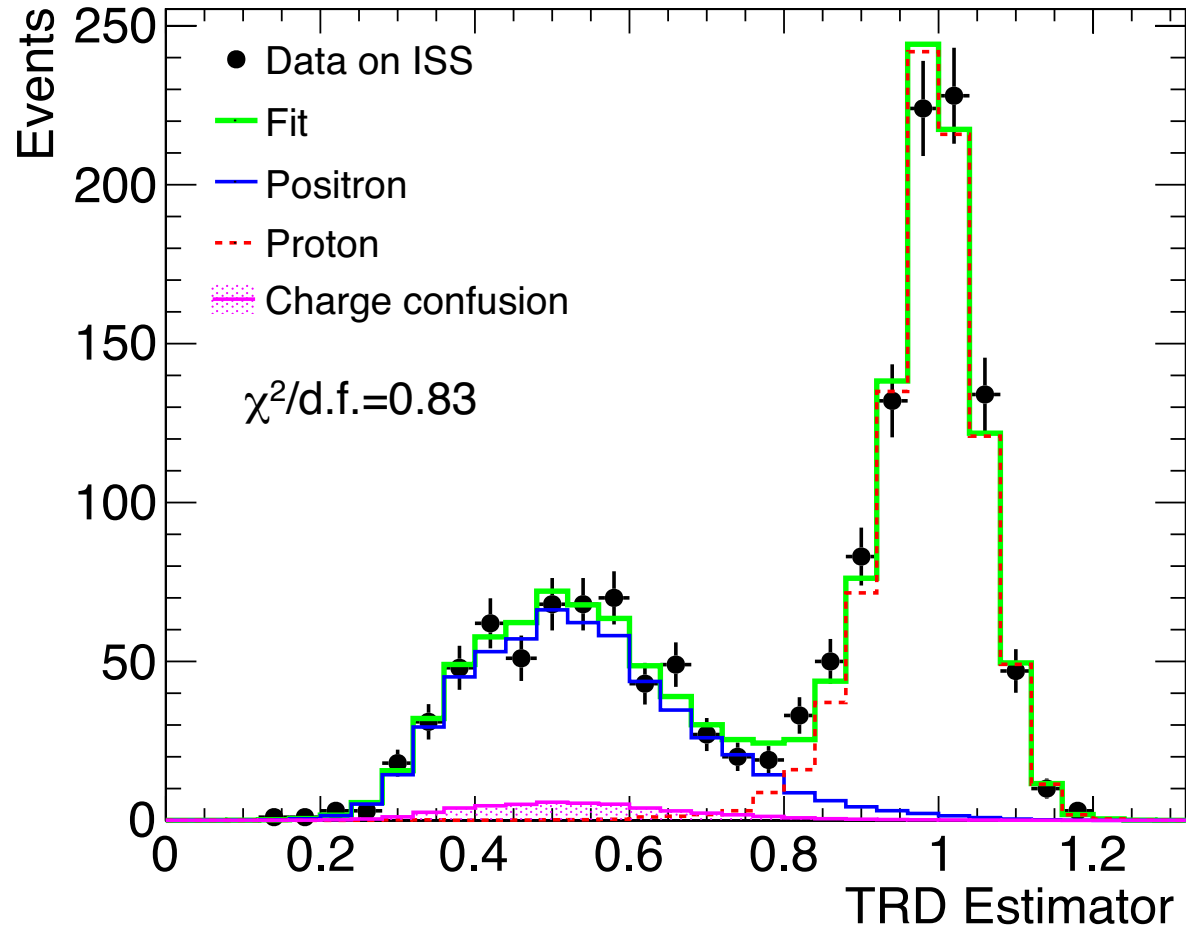
16

FIG. 3. Separation power of the TRD estimator in the energy range 83.2-100 GeV for the positively charged selected data sample. For each energy bin, the positron and proton reference spectra are fitted to the data to obtain the numbers of positrons and protons.
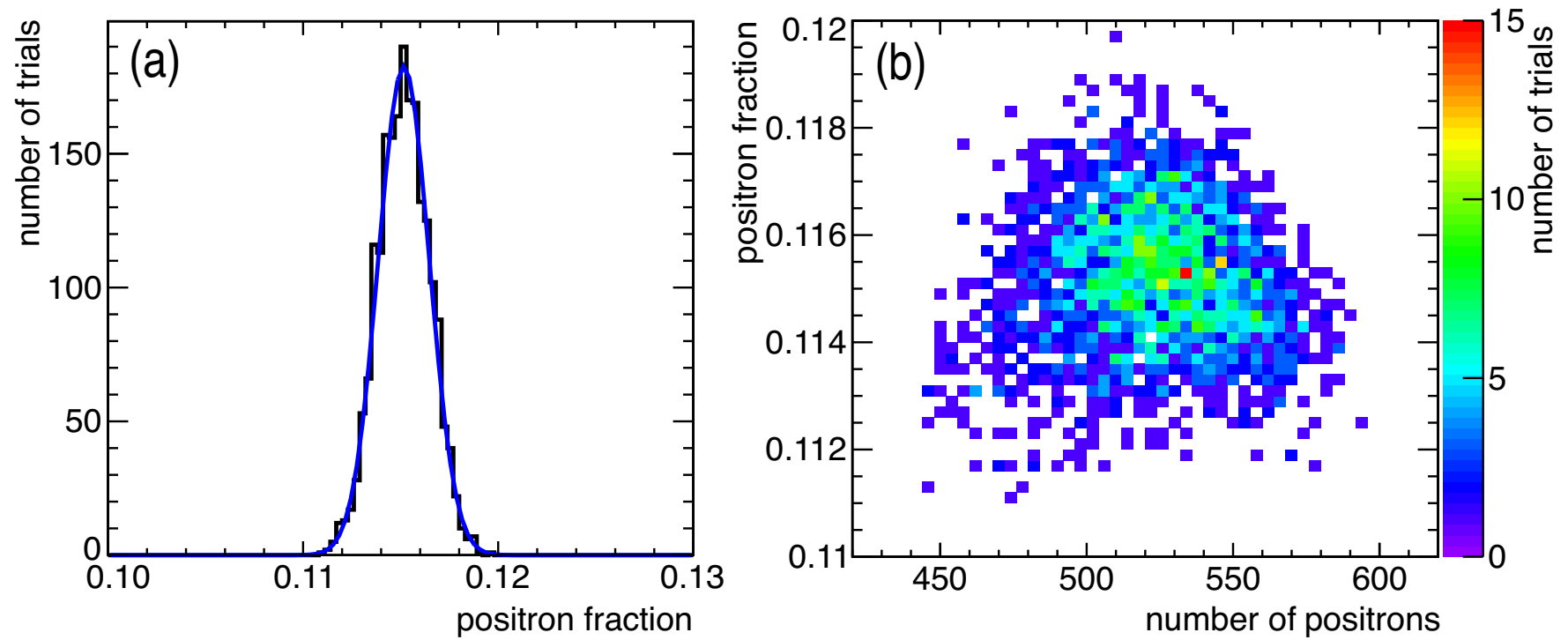
FIG. 4. (a) Stability of the measurement in the energy range 83.2-100 GeV over wide variations of the cuts fitted with a Gaussian of width 1.1 %. (b) The positron fraction shows no correlation with the number of selected positrons.
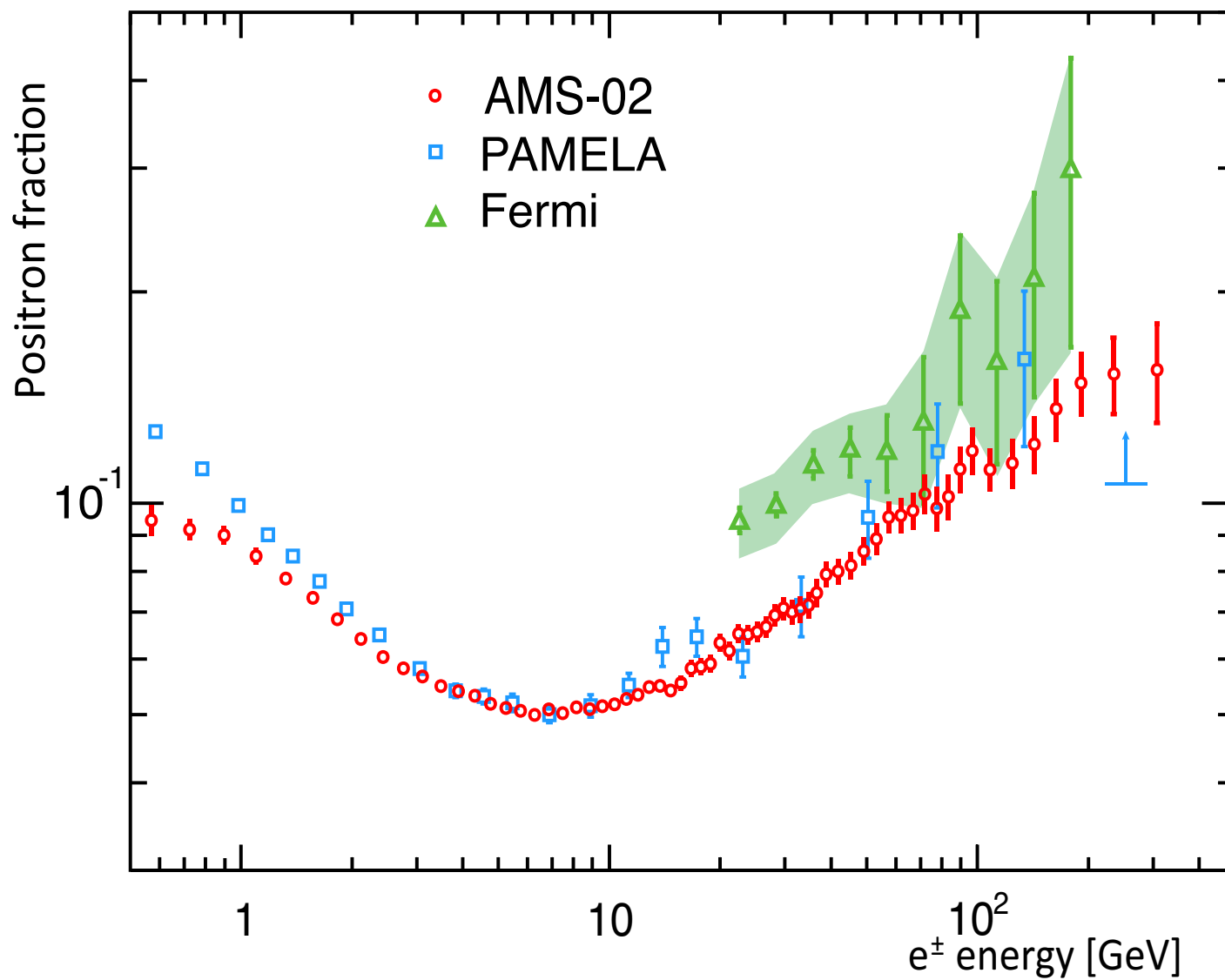
FIG. 5. The positron fraction compared with the most recent measurements from PAMELA [22] and Fermi-LAT [23]. The comparatively small error bars for AMS are the quadratic sum of the statistical and systematic uncertainties (see Table 1 and [13]) and the horizontal positions are the centers of each bin.
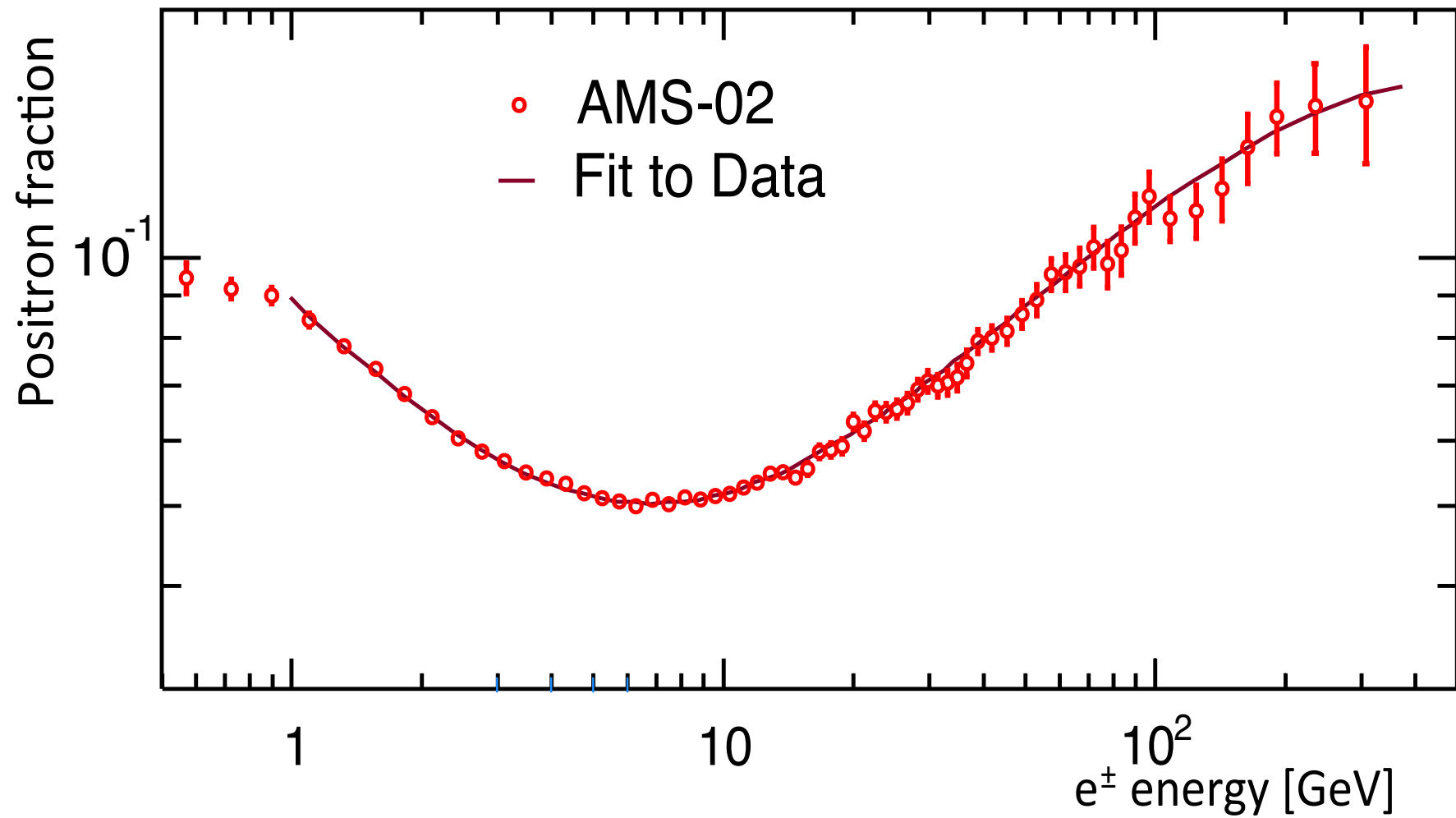
FIG. 6. The positron fraction measured by AMS fit with the minimal model. For the fit, both the data and the model are integrated over the bin width. Even with the high statistics and high accuracy of AMS, the spectrum shows no fine structure.